Modulating Bidirectional Catalytic Activity Through a RuNi Nanoalloy on Facile Candle Soot Carbon Towards Efficient Lithium-CO$_{2Mars}$ Batteries

Ankit Kumar Chourasia+,*[a] Keerti M. Naik+,[a] and Chandra S. Sharma*[a]

Lithium-CO$_2$ batteries have been at the forefront of reducing CO$_2$ emissions and addressing the present energy crisis. As the Martian atmosphere is 95% CO$_2$, this battery technology is ideal as a stand-alone energy storage device on the planet. However, challenges such as low reversibility, high charging voltages, and poor cycling life restrict its practicability. The current study addresses these by increasing the reversibility of the active reaction sites on the cathode via a synergistic interaction between the RuNi nanoparticle catalyst and candle soot carbon (CSC). This helps the system achieve a full discharge capacity of 15207 mAh g^{-1} at a high current density of 200 mA g^{-1} with 99.3% coulombic efficiency and an efficient cycling life of over 100 cycles at a higher current density of 500 mA g^{-1} for a limited capacity of 500 mAh g^{-1}. Further, combining ex-situ physical characterizations and density functional theory helps understand the underlying mechanism for improving the bidirectional CO$_2$ reduction and evolution activities during discharging and charging. The study, thus using a bimetallic catalyst and carbon, provides an approach for a single solution towards addressing the dual challenges of regulating CO$_2$ emissions on Earth and providing a constant energy source on Mars.

Introduction

The increased concentration of CO$_2$ in Earth's atmosphere necessitates the development of new technologies to mitigate and utilize the emitted CO$_2$.[1,2] Although technologies such as carbon capture and conversion of CO$_2$ to valuable fuels and chemicals have been developed in the recent past to achieve the target of reducing CO$_2$ emissions, these are more energy-intensive, inefficient, and still require much technological intervention.[3,4] Metal-gas batteries provide a unique opportunity to utilize the gas directly to generate electrical energy.[5,6] The development of Li-CO$_2$ battery technology may be an innovative approach for minimizing CO$_2$ emissions from the source (industries, power plants, etc.) by capturing CO$_2$ and electrochemically reducing it to generate and store electrical energy directly to meet the energy requirements.[7] In addition, the high energy density (1876 Wh kg^{-1}) of the Li-CO$_2$ battery compared with the conventional Li-ion batteries (~265 Wh kg^{-1}) provides a high specific energy alternative capable of mitigating CO$_2$ emissions at the same time.[8]

The desire to make Mars livable for human habitation has fascinated researchers for centuries. Martian atmosphere, comprising ~95% CO$_2$, provides natural operating conditions for utilizing the Li-CO$_2$ battery (Li-CO$_{2Mars}$) as an energy storage source for sustaining human activity. However, despite the advantages of Li-CO$_2$ batteries, several limitations, such as high charging voltage, low cycling stability, and poor reversibility when operated at different current densities, have limited their commercialization. The deposition of the insulating and highly stable discharge product, Li$_2$CO$_3$, on the cathode surface, blocking the gas diffusion into the system, has been the primary reason for the premature failure of the cell. The high thermodynamic barrier in decomposing Li$_2$CO$_3$ during charging can be overcome by developing catalysts that can reduce the activation energy for its decomposition.

Among the different electrocatalysts developed, carbon catalysts offer the advantage of low cost and high conductivity. However, their catalytic activity for CO$_2$ reduction and CO$_2$ oxidation is significantly low, necessitating their integration with catalysts that can enhance the activity of these electrochemical reactions. In this direction, transition metals, their oxides, sulfides, and carbides have been composited with different conductive carbons such as carbon nanotubes (CNT), graphene, and N-doped graphene for utilization as the cathode catalysts towards improving the performance of the Li-CO$_2$ battery.[9–17] Despite the increased performance of the batteries, the charging potential during cycling has been significantly high, which leads to its failure during long-term operation.

Due to their excellent catalytic activity, noble metal-based catalysts can be significantly utilized to overcome the limitations of decomposing the discharge products. Ru has been widely used for the electrochemical reduction of CO$_2$. Further, the charging potential decreases from ~4.3–4.5 V to ~3.6–3.8 V when using Ru as a catalyst. This signifies its ability to efficiently decompose the discharge products.[16,18] However, their high

[a] Mr. A. K. Chourasia,+ Dr. K. M. Naik,+ Prof. C. S. Sharma
Creative & Advanced Research Based On Nanomaterials (CARBON) Laboratory
Department of Chemical Engineering
Indian Institute of Technology Hyderabad
Kandi-502285, Sangareddy, Telangana (India)
E-mail: ch21resch01007@iith.ac.in
        cssharma@che.iith.ac.in
[+] These authors contributed equally to this work.

costs limit their use as individual catalysts, necessitating additional modification through different techniques. The combination of Ru with non-precious transition metals can be one such technique to develop a cost-effective catalyst for the Li-CO$_{2Mars}$ batteries. The alloying of two different metals to form a uniform-phase bimetallic alloy is a promising strategy to achieve it. The enhancement of its catalytic ability may be through electronic coupling or the strain arising in the nanostructures from the alloy formation.[19] Because of their similar redox potentials, Ni is the most advantageous transition metal for alloying with Ru atoms. In addition, Ni has been proven to be active for the electrochemical reduction of CO$_2$ and efficient decomposition of the discharge products in Li-CO$_2$ batteries.[20,21] However, due to the limited electronic conductivity of the nanoalloy metal catalysts and possible aggregation of the nanoparticles, the number of active catalytic sites is severely reduced, leading to lower catalytic activity.[22] This challenge can be solved by dispersing the nanoalloys on highly conductive carbon substrates. Thus, the interaction of the nanoparticles with the substrate may prevent the agglomeration of the nanoparticles. In addition, this will also ensure sufficient electronic conductivity for the efficient transfer of electrons from the reaction sites to the external circuit. Several highly conductive carbon substrates, ranging from single/multiwalled carbon nanotubes, graphene, reduced graphene-oxide, etc., have been widely used for anchoring the catalyst structures in Li-CO$_2$ batteries.[23–27] Despite their widespread utilization as carbon support for catalysts, the complexity associated with synthesizing such carbons and the high costs limit their application for scaling up the system. Ankit et al., in their study, demonstrated that uniformly distributed nano-sized carbon spheres, derived from the tip of the flame of a burning candle, can be efficiently utilized as a carbon catalyst compared to commercial multiwalled carbon nanotubes (MWCNT) for Li-CO$_{2Mars}$ batteries.[28] The exceptionally high surface area, comparable electronic conductivity, and interconnected network of the candle soot carbon (CSC) may provide the necessary characteristics for its utilization to anchor the bimetallic nanoalloys and provide a pathway for the efficient transport of electrons.

In our current study, we facilely synthesized RuNi nanoparticle alloys on the candle soot carbon as cathode catalysts for utilization in Li-CO$_{2Mars}$ batteries. The carbon-supported catalyst was developed using a two-step synthesis process involving the solvothermal method by a co-reduction process, leading to the development of the bimetallic catalyst on the candle soot. Further, calcination of the synthesized catalyst at 350 °C in Argon atmosphere induces ordering of the nanoparticles on the candle soot nanocarbon. Taking advantage of the increased catalytic activity from the electronic structure modification, the catalysts were employed for investigating the electrochemical performance of the Li-CO$_{2Mars}$ batteries. The batteries were observed to operate at a very low overpotential of ~1.7 V, even at a high current density of 500 mA g^{-1}. Also, the rate capability studies demonstrated that the system could be operated at a high current density of up to 1000 mA g^{-1} and efficiently reversed back to low current densities without any

significant loss in performance. Further, the batteries can be completely discharged to a capacity of 15207 mAh g^{-1} and a reversible charge capacity of 15185 mAh g^{-1} at the current density of 200 mA g^{-1} with 99.3% coulombic efficiency. In addition, the long-term cycling performance of the battery using the RuNi/CSC catalyst can be efficiently cycled to over 100 cycles with the overpotential of ~1.9 V at the 100th cycle at a high current density of 500 mA g^{-1} with a discharge/charge capacity limitation of 500 mAh g^{-1}. Furthermore, the catalytic effect on the efficient reversibility of the active reaction sites was established by ex-situ X-ray diffraction (XRD), X-ray photoelectron spectroscopy (XPS), field emission scanning electron microscopy (FESEM), transmission electron microscopy (TEM) and Raman characterizations of the cathodes at different stages of battery operation. The density functional theory (DFT) studies show that due to the RuNi/CSC catalyst, the discharge reaction proceeds through anchoring the Li ions on the active sites, followed by CO$_2$ adsorption. Also, the formation reaction of Li$_2$C$_2$O$_4$, being the kinetically limiting discharge step, was possibly the reason for the high performance of the RuNi/CSC catalyst-based Li-CO$_{2Mars}$ battery. Further, the lower thermodynamic barrier for the decomposition of the discharge product using RuNi/CSC catalyst signifies the excellent catalytic activity towards the reversibility of the batteries.

Results and Discussion

Structural characterization of the catalyst

The RuNi/CSC alloy catalyst was prepared by the solvothermal method, as depicted in Figure 1(a). Briefly, the candle soot carbon (CSC) was dispersed in the ethylene glycol solvent, followed by the addition of the catalyst precursors, ruthenium (III) chloride hydrate (RuCl$_3 \cdot$3H$_2$O) and nickel (II) nitrate hexahydrate (Ni(NO$_3$)$_2 \cdot$6H$_2$O). The hydrothermal reaction was then carried out at 180 °C for 10 hours to obtain the nanoalloy dispersed on CSC. The residue obtained was subsequently heat treated at 350 °C for 2 hours in an Argon atmosphere, leading to the formation of the alloy RuNi on CSC.

The structural properties of the synthesized catalyst and the formation of RuNi nanoalloy were confirmed by XRD studies. The presence of hexagonal close-packed diffraction peaks of Ru confirms its existence in the RuNi nanoalloy. Further, the shift in the Ru (101) peak at 44° and merging with the Ni (111) peak at 44.5° to form a broader peak confirms the incorporation of Ni in the lattice of Ru, forming the nanoalloy (Figure 1b). This peak is distinct from the sharp peak observed in the case of Ru/CSC at 44°. Furthermore, when the peaks of the synthesized catalyst were compared to the standard pattern of RuNi (JCPDS-03-065-6490), the peaks matched with a minor shift to higher angles, indicating a variable ratio of the component metals. In addition, the broad carbon peak (002) at 25.3° is negatively shifted to a lower angle compared to the standard peak of 26.4° (JCPDS: 00-001-0640) of graphite, indicating the increase in the graphitization of the carbon and synergistic interaction between the substrate CSC and the bimetallic RuNi nanoparticles. Further, it
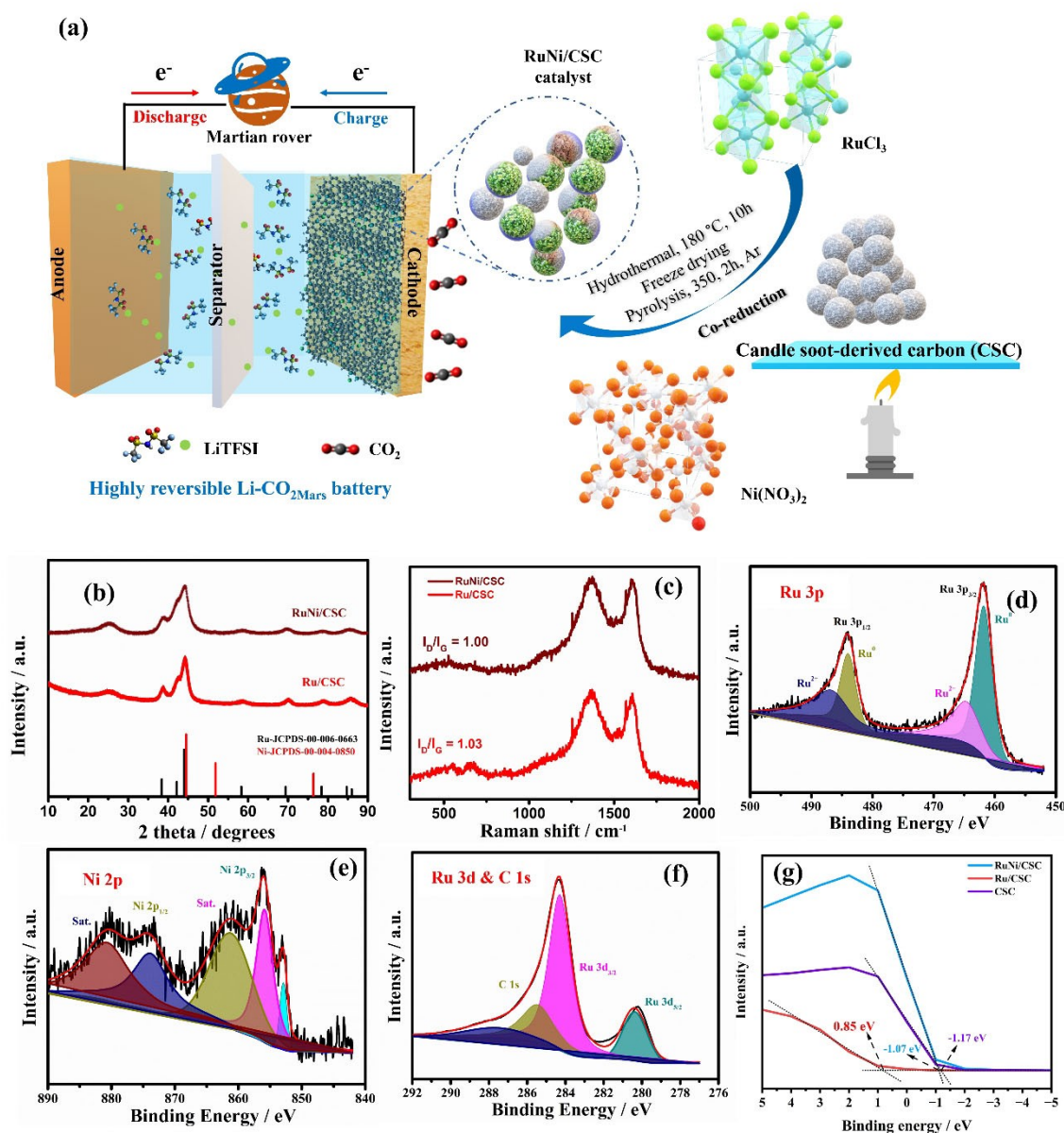
Batteries & Supercaps

Research Article
doi.org/10.1002/batt.202300328

Chemistry Europe
European Chemical
Societies Publishing

Figure 1. a) Schematic illustration of the RuNi/CSC catalyst synthesis for use as a cathode in the Li-CO$_{2Mars}$ battery. b) XRD, c) Raman spectra of RuNi/CSC and Ru/CSC. d) Ru 3p, e) Ni 2p, f) Ru 3d and C 1s XPS spectra of the RuNi/CSC catalyst. g) XPS valence band spectra of the RuNi/CSC, Ru/CSC, and CSC catalysts.

can be observed the broadness of the (002) plane of carbon is reduced in RuNi/CSC compared to the Ru/CSC catalyst arising from the incorporation of Ni atoms in the Ru lattice, leading to a modified electronic structure of the composite that contributes to an improved catalytic activity of the bimetallic nanoalloy carbon catalyst (Figure 1b).

Raman spectroscopy studies were carried out to investigate the effect on the displacement of the intralayer and interlayer chemical bonds in the carbon structure due to the anchoring of the RuNi nanoparticles. As we can observe from Figure 1(c), there is a reduction in the I_D/I_G ratio for the RuNi/CSC catalyst compared to the Ru/CSC catalyst. The I_D and I_G bands are related to the intensity of the D and G band peaks, respectively.

The D band at 1356 cm^{-1} corresponds to the out-of-plane vibrations in the aromatic rings arising from structural and edge defects for the sp^2 carbon. The G band at 1602 cm^{-1} relates to the in-plane vibrations of the aromatic rings due to the graphitic content. The I_D/I_G ratio quantifies the degree of ordering in the carbon-related systems. The reduced ratio observed with the incorporation of RuNi on the CSC suggested the enhanced stacking of the graphitic layers of the CSC leading to an increase in the degree of graphitization of the composite catalyst along with the modified electronic structure of the composite catalyst. The increased graphitization and the altered electronic structure of the catalyst facilitates the efficient transfer of electrons and increased catalytic activity.

The chemical composition and electronic structures of the RuNi/CSC catalyst were then investigated through XPS. The observation of Ru 3p, Ru 3d, Ni 2p, and C 1s in the wide XPS spectra confirmed their presence in the synthesized catalyst (Figure S1). The core spectrum of Ru 3p exhibits the presence of the doublets of Ru $3p_{1/2}$ and Ru $3p_{3/2}$ states at the binding energies of 487.7 eV and 463.8 eV, respectively (Figure 1d). The deconvolution of the Ru $3p_{1/2}$ peak results in two peaks at 484.1 eV and 487.1 eV, attributed to the binding energies of the Ru^0 and Ru^{2+}, respectively. Similarly, the Ru $3p_{3/2}$ peaks were deconvoluted to Ru^0 and Ru^{2+} peaks at 461.9 eV and 464.9 eV, respectively. When matched with the standard peaks of Ru^0 $3p_{1/2}$ and Ru^0 $3p_{3/2}$, it can be observed that there was a shift towards lower binding energy in the synthesized RuNi/CSC catalyst. The shift arises due to the electron transfer from the lesser electronegative Ni (1.9) to the more electronegative Ru (2.2), indicating the alloying of Ru with Ni metal. The Ni 2p spectra can be deconvoluted into Ni $2p_{1/2}$ and Ni $2p_{3/2}$ peaks at 874.2 eV and 856.0 eV, respectively. The deconvoluted peaks matching with the standard peaks can be observed to be shifted towards increasing binding energy, confirming the electron transfer from Ni to Ru for the formation of RuNi catalyst (Figure 1e). The C 1s and Ru 3d spectra have been fitted together due to their overlapping chemical states. The Ru 3d spectra were deconvoluted to Ru $3d_{3/2}$ and Ru $3d_{5/2}$ at the peak value of 284.3 eV and 280.4 eV, respectively.

Further, the deconvolution of C 1s spectra at the peaks of 287.8 and 285.5 eV corresponding to the C=O and sp^2-C carbon, respectively, indicates the interaction of the RuNi with CSC to give the composite nanoalloy RuNi/CSC catalyst (Figure 1f). Additionally, to understand the change in the electronic structure of the catalyst from the alloying of the two metals, valence band spectra (VBS) were obtained by employing the high-resolution XPS. As can be observed in Figure 1(h), there was a shift in the valence band towards negative binding energy from that for CSC, indicating the metallic alloy nanoparticle formation enhances the conductivity. Further, compared to Ru/CSC, the valence band is shifted towards the Fermi level, from −1.17 eV for Ru/CSC to −1.07 eV for RuNi/CSC, leading to an enhanced electronic conductivity of the composite catalyst. After confirmation of the nanoalloy's formation and change in electronic state, the composition of the catalyst was determined.

In the synthesized RuNi/CSC catalyst, the Ru to Ni composition ratio, as calculated from the XPS spectra, was found to be 2.9:1 (74.4% Ru and 25.6% Ni), which was further confirmed through inductively coupled plasma-optical emission spectroscopy (ICP-OES) and found to be similar. The mass loading of the catalyst onto the candle soot carbon substrate was around 26.4%, the rest being carbon.

To understand the formation and morphology of the formed RuNi on candle soot carbon nanocarbons, FESEM and TEM studies were carried out. It can be observed from the FESEM images that the nanospherical particles of CSC were uniformly distributed and connected with a granular covering on the surface (Figure 2a, S2). Furthermore, it can be shown from the elemental mapping generated by energy-dispersive x-ray spectroscopy that the elements Ru and Ni are evenly
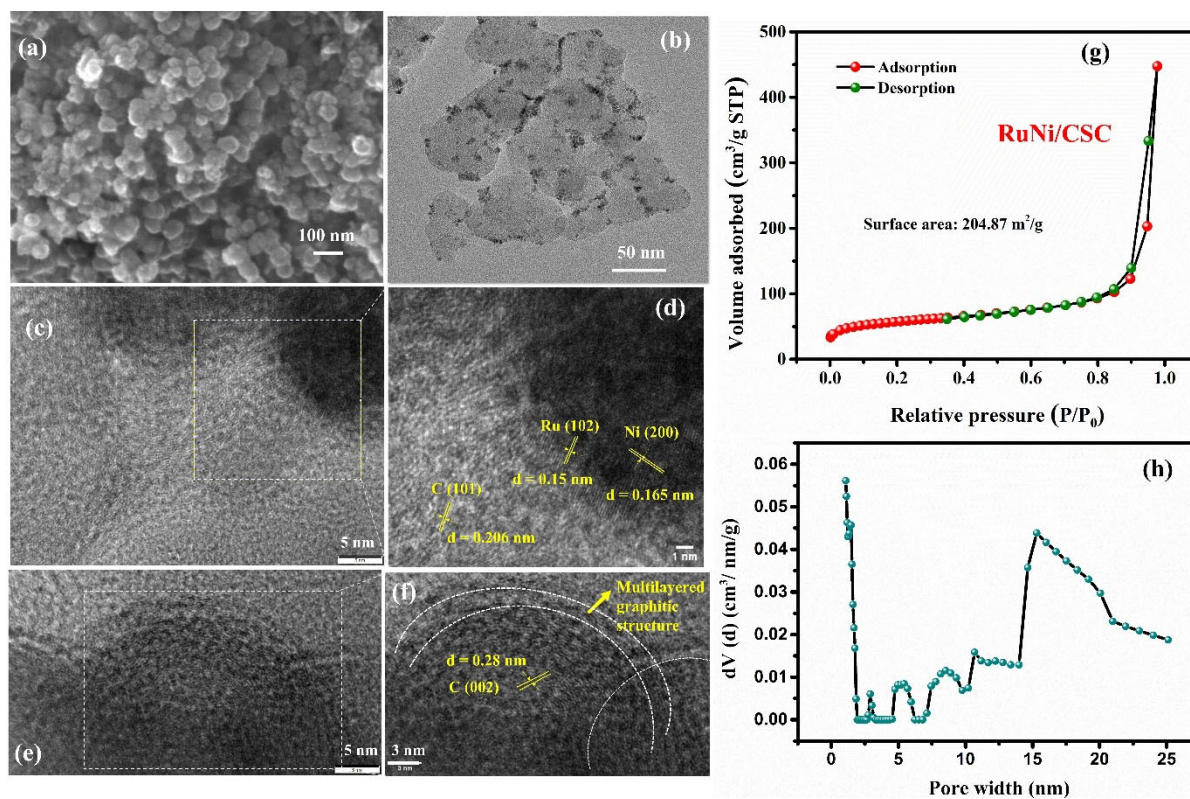

Figure 2. a) FESEM, b) TEM, c–f) HRTEM images, g) N$_2$ adsorption-desorption isotherm and h) pore size distribution of the synthesized RuNi/CSC catalyst.

Batteries & Supercaps

Research Article
doi.org/10.1002/batt.202300328

Chemistry Europe
European Chemical
Societies Publishing

dispersed on the substrate carbon with no aggregation of the synthesized catalyst (Figure S3). Further, from the TEM images, it can be observed there was a uniform distribution of RuNi nanoparticles on the interconnected CSC nanospheres. (Figure 2b) In comparison, the Ru nanoparticles were aggregated on the substrate carbon due to their higher surface energy. (Figure S4) The HRTEM images of the synthesized RuNi/CSC confirm the formation of Ru and Ni nanoalloy with Ru (102) and Ni (200) planes. The C (101) plane observed in the composite catalyst confirms the synergistic interaction between the RuNi and the CSC. Additionally, the enhancement in the graphitic structure of CSC due to the incorporation of RuNi can be observed with the increased ordering of the graphitic layers compared to the Ru/CSC catalyst. (Figures 2c–f, S5)

The N_2 adsorption-desorption studies were further carried out to investigate the surface area and the pore size distribution of the synthesized catalysts. The host CSC has a very high surface area of 640.6 $m^2 g^{-1}$, thus providing a larger space for the catalysts to anchor on it. Further, despite the reduction in the surface area of the composite catalyst from the incorporation of the Ru (314.7 $m^2 g^{-1}$) and RuNi (204.87 $m^2 g^{-1}$) nanoparticles, it was still significantly higher. In addition, it can be

observed that the composite catalysts were mesoporous compared to the microporous nature in the CSC (Figures 2g and h, S6). The high surface area with the modified pore structure will be advantageous towards increased reactivity for the CO_2RR and CO_2ER, along with enhanced interaction between the reactants.

Electrochemical performance of the Li-CO$_{2Mars}$ battery

Electrochemical studies were carried out to study further the different synthesized catalysts' catalytic activity and their influence as a cathode catalyst on the operational ability of the Li-CO$_{2Mars}$ battery. The CO_2 reduction and evolution activity needs to be explored before assessing the catalyst's impact on the Li-CO$_{2Mars}$ battery's performance. It can be observed from the cyclic voltammetry curves that CO_2 reduction peaks can be detected at the potential of 2.28 V for the RuNi/CSC nanoalloy catalysts, with slightly higher potentials for the counter materials Ru/CSC and CSC catalysts. However, as can be seen from Figure 3(a), the peak current increased with the addition of Ru to CSC, and further enhancement was observed in the
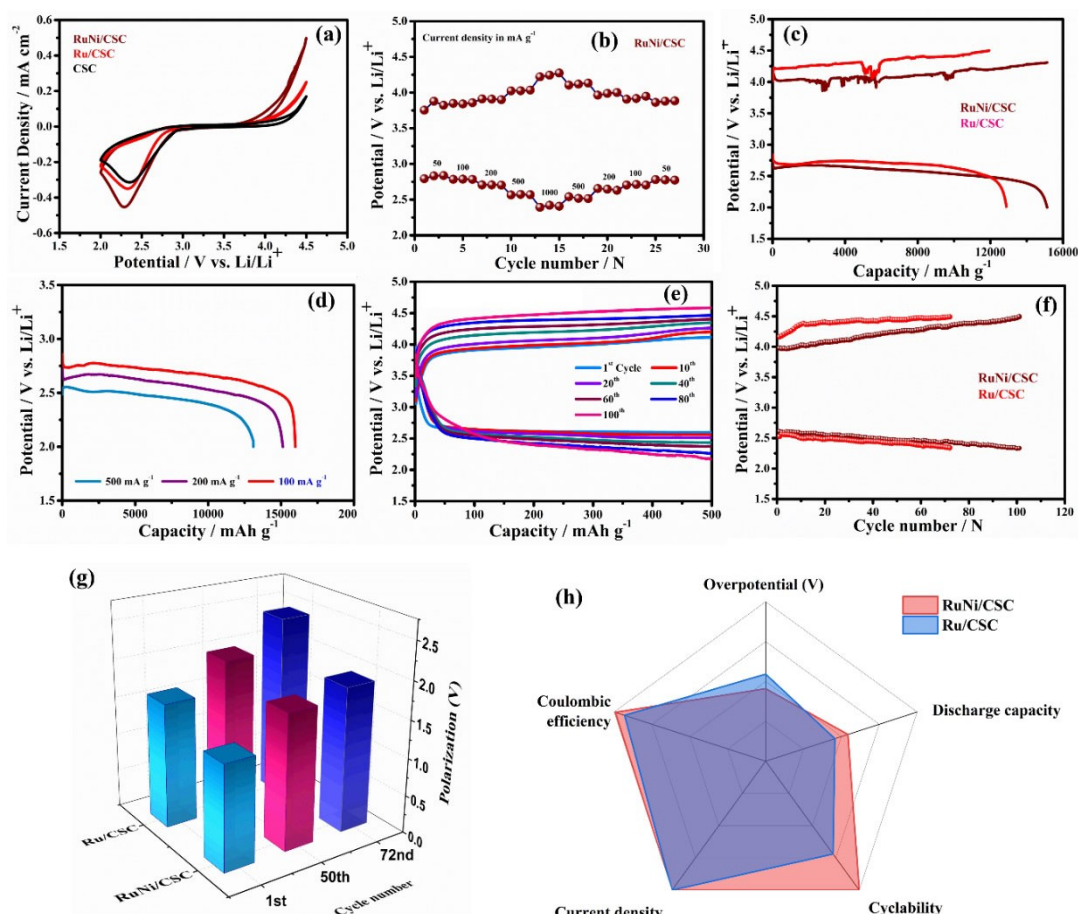

Figure 3. a) Cyclic voltammograms at a scan rate of 0.1 mV s^{-1}. b) Rate capability study for the catalyst RuNi/CSC. c) Galvanostatic full discharge and charge curves for the RuNi/CSC and Ru/CSC at the current density of 200 mA g^{-1}. d) Full discharge at different current densities of 100, 200 & 500 mA g^{-1}. e) Cyclability at 500 mA g^{-1} for the RuNi/CSC-based Li-CO$_{2Mars}$ battery. f) The potential vs. cycle plot for RuNi/CSC and Ru/CSC catalyst-based batteries at the current density of 500 mA g^{-1}. g) A comparison of the overpotential for RuNi/CSC and Ru/CSC catalysts in the 1st, 50th, and 72nd cycle. h) Radar chart comparing the different parameters for suitability of catalyst in Li-CO$_{2Mars}$ battery.

case of the RuNi/CSC catalyst. This indicates the better catalytic activity of RuNi/CSC catalyst than when using Ru alone as the catalyst site. Further, the higher onset reduction and lower oxidation potentials leading to low overpotential (difference between the onset reduction and oxidation potentials) suggest enhanced CO_2 reduction and oxidation activity. The rate capability studies were conducted to investigate the ability to operate the batteries at different current densities ranging from 50–1000 mA g^{-1} to a limited capacity of 500 mAh g^{-1} (Figure 3b). When using RuNi/CSC as the cathode catalyst, there was a slight increase in the overpotential of the batteries with the increase in current density. The voltages recovered to initial operating potentials, as the current density was reversed from 1000 mA g^{-1} to 50 mA g^{-1}. In the case of Ru/CSC and CSC as catalysts, a similar trend was observed with a higher overpotential compared to RuNi/CSC catalyst. However, due to their limited catalytic ability, the batteries with Ru/CSC and CSC as cathode catalysts could not be operated at 1000 mA g^{-1} (Figure S7).

The full discharge and charge capacities of the Li-CO_{2Mars} battery were determined in the voltage range of 2–4.5 V. The Li-CO_{2Mars} battery showed an impressive full discharge capacity of 15207 mAh g^{-1} at a current density of 200 mA g^{-1}. The discharge potential was greater than 2.5 V, and a nearly 99.3% reversible charge capacity of 15185 mAh g^{-1} was obtained at a charging potential of ~4.3 V. In comparison, the Ru/CSC catalyst-based Li-CO_{2Mars} battery could discharge only 12772 mAh g^{-1} at the current density of 200 mA g^{-1} with a coulombic efficiency of 91.9% (Figure 3c). Despite comparable coulombic efficiency to RuNi/CSC, the lower discharge capacity and the high overpotential affirm the improvement in the catalytic activity due to the addition of Ni and the formation of nanoalloy.

Furthermore, for the RuNi/CSC-based catalyst, no significant change was observed in the achievable discharge capacity from the variation in the current density from 100 mA g^{-1} to 200 mA g^{-1}. Subsequently, even at a high current density of 500 mA g^{-1}, the achievable discharge capacity was significantly higher at 13125 mAh g^{-1} signifying the excellent catalytic activity of the RuNi/CSC nanoalloy catalyst (Figure 3d). Having explored the maximum achievable discharge capacities at different current densities, we examined the cycling performance of the cells for a limited capacity of 500 mAh g^{-1} with the catalysts, i.e., RuNi/CSC and Ru/CSC, based Li-CO_{2Mars} battery. The RuNi/CSC cathode catalyst-based Li-CO_{2Mars} battery displayed an impressive discharge potential of ~2.7 V. In comparison, the charging potential was significantly reduced to 3.8 V, thus having a very low overpotential of 1.1 V at the current density of 200 mA g^{-1}. The battery could be cycled up to 85 cycles with a gradual increase in the overpotential from (1.14 V) in the first cycle to (1.8 V) in the 85th cycle (Figure S8). Further, cycling at an increased current density of 500 mA g^{-1} for the same limited capacity improved the cyclability of the battery to 100 cycles with a slight decrease in the discharge and an increase in the charge potential (Figure 3e and f). Compared to the RuNi/CSC catalyst, the Ru/CSC catalyst-based Li-CO_{2Mars} battery could only cycle up to 60 cycles at 200 mA g^{-1}

and 70 cycles at 500 mA g^{-1} (Figure S9). Also, the polarization was significantly lower for RuNi/CSC compared to Ru/CSC at similar cycle numbers (Figure 3g). The carbon substrate, CSC, has a cyclability of nearly 60 cycles at the current density of 200 mA g^{-1} with a significantly higher overpotential than Ru/CSC or RuNi/CSC catalyst (Figure S10). Due to its low catalytic ability to reversibly decompose the discharge product, CSC could not be cycled at the high current density of 500 mA g^{-1}. This indicates the improvement in the performance was through the incorporation of noble metal-based catalysts. The effect of alloying the two metals and its impact on the overall performance of the Li-CO_{2Mars} battery was evidenced by the outstanding catalytic ability of the RuNi/CSC catalyst compared to Ru/CSC and other reported catalysts in literature for Li-CO_2 batteries (Figure 3h, Table S1).

Understanding the reaction mechanism

Physical characterization

The improved performance of the Li-CO_{2Mars} battery using RuNi/CSC as the cathode catalyst requires further understanding of the reaction mechanism and the state of the cathode surface as the battery is operated. Electrochemical impedance spectroscopy provides a unique approach to investigating the state of the cathode as it is discharged and charged back. It can be observed from the electrochemical impedance spectra that the discharged electrode had an increased charge transfer resistance, evidenced by the semi-circular part of the curve.

The increased resistance to the charge transfer was due to the accumulation of the insulating discharge products, Li_2CO_3, and amorphous carbon on the catalyst surface, leading to its deactivation. On charging back, the interfacial charge transfer and diffusion resistance were reduced and was closer to that of the pristine electrode, signifying the decomposition of Li_2CO_3 leading to CO_2 evolution. In contrast, for the Ru/CSC catalyst, there was a significant increase in the charge transfer resistances, indicating the poor reversibility of the battery. This demonstrates the effect of RuNi/CSC alloy on the performance of the Li-CO_{2Mars} battery (Figure S11). The Li-CO_{2Mars} batteries were disassembled to get the discharged and charged electrodes, which were analyzed by ex-situ XRD, Raman spectroscopy, XPS, and FESEM techniques to develop a better understanding of the mechanism of the formation and decomposition of the reaction products. The discharge product Li_2CO_3 peaks can be observed from the XRD patterns in the discharged electrode, which disappeared completely on charging back the system (Figure 4a). Additionally, when comparing the XRD patterns of the pristine and charged electrodes, the peaks of the nanoalloy RuNi/CSC catalyst showed no alteration, indicating that the catalyst's structure remained stable throughout battery operation. Whereas, for the Ru/CSC catalyst-based Li-CO_{2Mars} battery, it can be observed that the charging back of the electrodes did not lead to the complete decomposition of the discharge product Li_2CO_3, confirming the observance of a higher over-
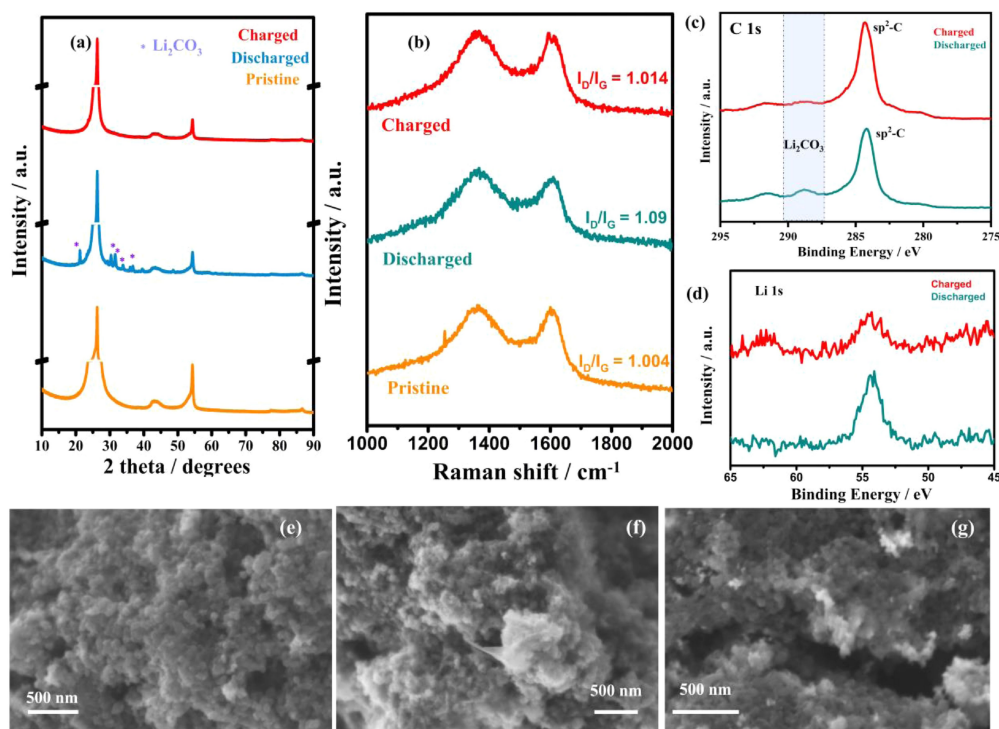
Figure 4. a) XRD pattern, b) Raman spectra of pristine, discharged, and charged electrodes. c) C 1s, d) Li 1s XPS spectra of the discharged and charged electrodes. FESEM images of the e) pristine, f) discharged, and g) charged electrodes.
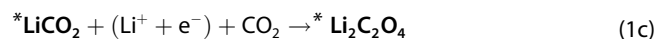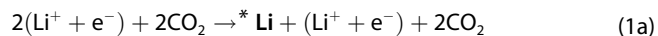
potential for the monometallic catalyst-based battery (Figure S12a).
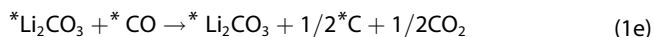
Raman spectroscopy studies were further carried out to investigate the formation and reversibility of the amorphous carbon and Li_2CO_3 formed during the discharge reaction. It can be observed from the Raman spectra in Figure 4(b) that the I_D/I_G ratio increased from 1.004 in the pristine state to 1.09, indicating the formation of amorphous carbon. The subsequent charging of the battery leads to a reduction in the I_D/I_G ratio to 1.014, similar to the pristine state, indicating the decomposition of formed amorphous carbon along with Li_2CO_3. Comparatively, for the Ru/CSC catalyst, the charging back of the system although led to a decrease in the ratio, it was significantly higher than that in the pristine state suggesting the incomplete decomposition of the discharge products (Figure S12b). High-resolution C 1s and Li 1s XPS spectra were observed for the discharged and the charged electrodes of RuNi/CSC. The observable peak at 288.8 eV and 291.6 eV corresponding to the C=O in the C 1s spectrum can be attributed to the formation of the discharge product Li_2CO_3 on discharging, which almost disappears completely when the battery is charged. Further, from the Li 1s spectra, the Li peak at 54.4 eV confirmed the formation of the discharge product Li_2CO_3, which on charging almost completely disappeared, indicating the decomposition of Li_2CO_3 into Li^+ ions and CO_2 molecules as per the reaction, $2Li_2CO_3 + C$ (amorphous)$\rightarrow 4Li^+ + 3CO_2 + 4e^-$ (Figure 4c, d). It can be observed from the FESEM images that the RuNi/CSC nanospheres were covered with flower-like morphology discharge product covering the active site, limiting the discharge reaction in the system (Figure 4e, f). Contrarily, for the Ru/CSC-

based system, thick film-like coverage along with the formation of the crystalline aggregates are observed, leading to faster deactivation of the active sites (Figure S13a, b). Further, the charging of the RuNi/CSC electrodes leads to almost complete decomposition of the discharge product with the regeneration of the active sites for the CO_2 reduction reaction (Figure 4g). In the case of the Ru/CSC, despite the recovery of the active sites, significant discharge products can be observed to be present, limiting the regeneration of the active sites (Figure S13c). The observations from the various structural and morphological characterization techniques demonstrate the ability of the RuNi/CSC catalyst to efficiently reverse the discharge products and thus improve the electrochemical performance of the Li-CO_{2Mars} battery.

DFT simulation studies

The first principle DFT calculations were carried out to obtain a clear mechanistic insight into the high performance of the RuNi/CSC catalyst. As per a study by Guo et al.,[29] the discharge reaction in catalysts can be predicted to proceed as per the reaction pathway in Equation (1).

$$2(Li^+ + e^-) + 2CO_2 \rightarrow {}^*Li + (Li^+ + e^-) + 2CO_2 \tag{1a}$$

$${}^*Li + (Li^+ + e^-) + 2CO_2 \rightarrow {}^*LiCO_2 + (Li^+ + e^-) + CO_2 \tag{1b}$$

$${}^*LiCO_2 + (Li^+ + e^-) + CO_2 \rightarrow {}^*Li_2C_2O_4 \tag{1c}$$

$$*Li_2C_2O_4 \rightarrow{}^* Li_2CO_3 +{}^* CO \tag{1d}$$

$$*Li_2CO_3 +{}^* CO \rightarrow{}^* Li_2CO_3 + 1/2{}^*C + 1/2CO_2 \tag{1e}$$

It has been perceived that the discharge reaction proceeds with the physical adsorption of CO_2 onto the catalyst site. However, in the case of the RuNi/CSC catalyst, the discharge reaction proceeds with the anchoring of Li^+ ion on the catalyst site rather than the adsorption of CO_2 observable from the positive adsorption energy of CO_2 on the catalytic sites. The anchoring of Li^+ ions on the catalyst surface possibly modulates the electronic structure of the active site. It enhances the adsorption of CO_2 on the site, forming the discharge product intermediate $*LiCO_2$, where $*$ indicates the adsorbed species on the catalyst. The following steps involving the intermediates' formation and relative stabilities in the discharge reactions determine the system's achievable discharge capacity and stability during discharge. It can be observed from the

theoretical calculations that the next step of the formation of $*Li_2C_2O_4$ was the kinetically limiting step and was possibly the reason for the excellent performance of the RuNi/CSC-based Li-CO_{2Mars} battery compared to that of the Ru/CSC catalyst. The next step of the disproportionation of $Li_2C_2O_4$ into $*Li_2CO_3$ and $*CO$ was thermodynamically favorable and confirmed the experimental evidence of the Li_2CO_3 as the discharge product.

Further reduction of the adsorbed $*CO$ to C was uphill; thus, the reaction's final step was energy consuming, resulting in a slight drop in the discharge potential (Figure 5a and b, Table S2). The positive adsorption energy signified the difficulty in forming amorphous carbon, thus reducing the deactivation of the active sites and higher performance of the RuNi/CSC battery. In contrast, the formation of carbon was easier in Ru/CSC than in RuNi/CSC due to the lower positive adsorption energy. This leads to faster deactivation of the active sites, resulting in the poor performance of the battery. The charging process in Li-CO_2 batteries has been a major concern, owing to the reluctant decomposition of the discharge products formed
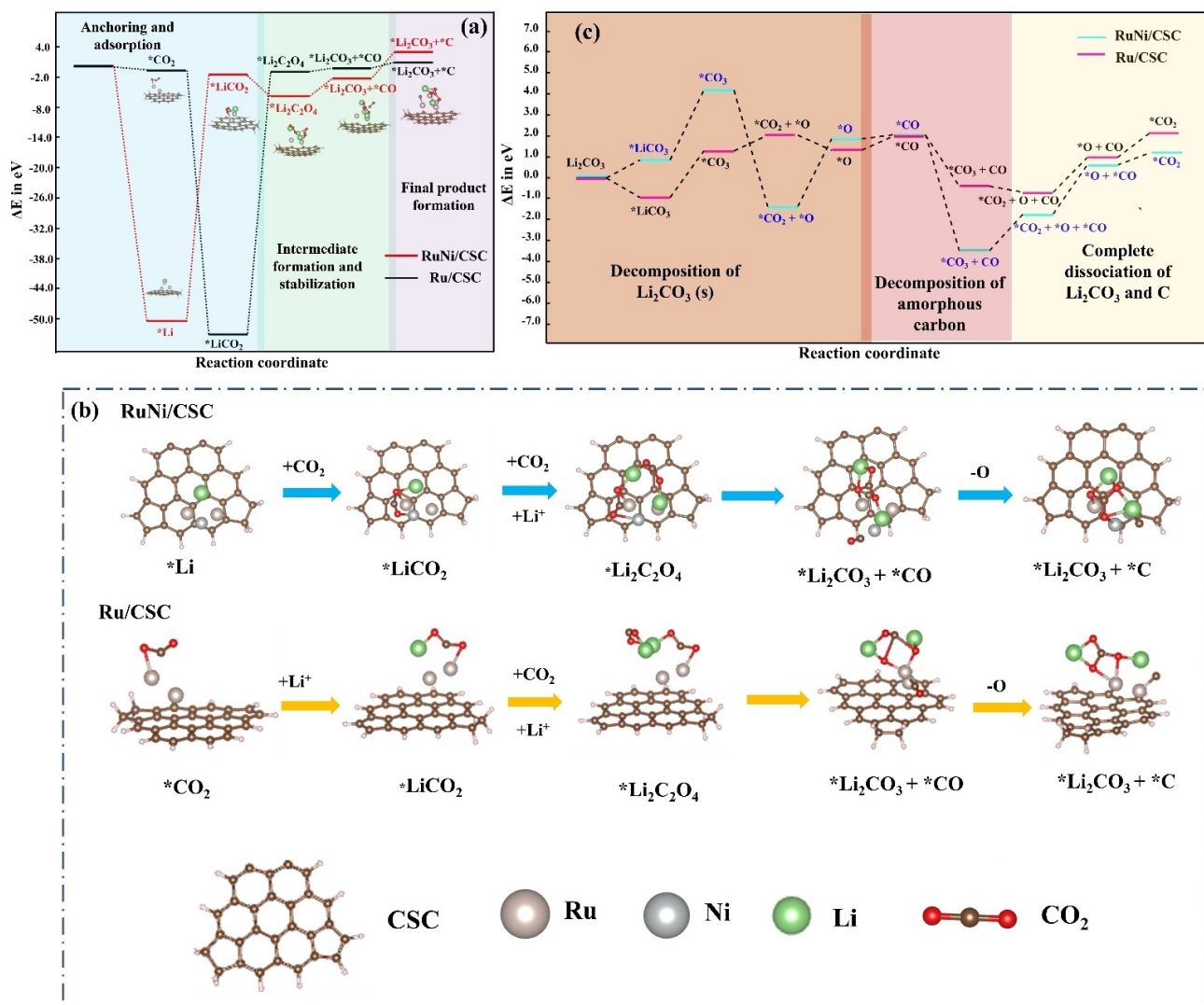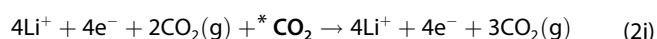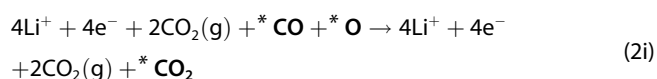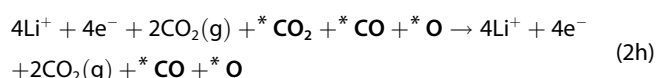

Figure 5. a) Discharge reaction profile and b) the reaction pathway for RuNi/CSC and Ru/CSC catalyst. c) Charge reaction profile with changes in adsorbed energy for the RuNi/CSC and Ru/CSC catalyst.

Batteries & Supercaps

Research Article
doi.org/10.1002/batt.202300328

Chemistry Europe
European Chemical
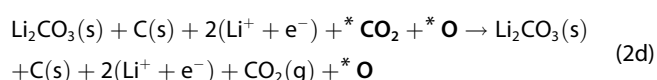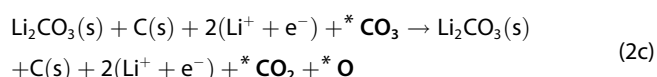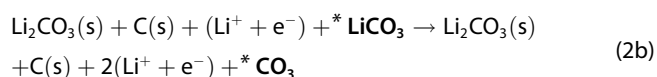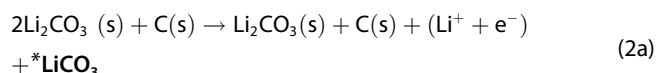Societies Publishing

during the discharge process. Thus, understanding the reaction mechanisms during the charging process is also essential. As confirmed by the experimental observations, there was significant evidence of the decomposition of Li_2CO_3 and amorphous carbon. Thus, the overall charge reaction can be confirmed as $2Li_2CO_3 + C \rightarrow 4Li^+ + 3CO_2 + 4e^-$. The charging reaction can be estimated to have the reaction pathway per the reactions in Equation (2).

$$2Li_2CO_3\ (s) + C(s) \rightarrow Li_2CO_3(s) + C(s) + (Li^+ + e^-) +\ ^*\mathbf{LiCO_3} \tag{2a}$$

$$Li_2CO_3(s) + C(s) + (Li^+ + e^-) +\ ^*\mathbf{LiCO_3} \rightarrow Li_2CO_3(s) + C(s) + 2(Li^+ + e^-) +\ ^*\mathbf{CO_3} \tag{2b}$$

$$Li_2CO_3(s) + C(s) + 2(Li^+ + e^-) +\ ^*\mathbf{CO_3} \rightarrow Li_2CO_3(s) + C(s) + 2(Li^+ + e^-) +\ ^*\mathbf{CO_2} +\ ^*\mathbf{O} \tag{2c}$$

$$Li_2CO_3(s) + C(s) + 2(Li^+ + e^-) +\ ^*\mathbf{CO_2} +\ ^*\mathbf{O} \rightarrow Li_2CO_3(s) + C(s) + 2(Li^+ + e^-) + CO_2(g) +\ ^*\mathbf{O} \tag{2d}$$

$$Li_2CO_3(s) + C(s) + 2(Li^+ + e^-) + CO_2(g) +\ ^*\mathbf{O} \rightarrow Li_2CO_3(s) + 2(Li^+ + e^-) + CO_2(g) +\ ^*\mathbf{CO} \tag{2e}$$

$$Li_2CO_3(s) + 2(Li^+ + e^-) + CO_2(g) +\ ^*\mathbf{CO} \rightarrow 4Li^+ + 4e^- + CO_2(g) +\ ^*\mathbf{CO_3} +\ ^*\mathbf{CO} \tag{2f}$$

$$4Li^+ + 4e^- + CO_2(g) +\ ^*\mathbf{CO_3} +\ ^*\mathbf{CO} \rightarrow 4Li^+ + 4e^- + CO_2(g) +\ ^*\mathbf{CO_2} +\ ^*\mathbf{CO} +\ ^*\mathbf{O} \tag{2g}$$

$$4Li^+ + 4e^- + 2CO_2(g) +\ ^*\mathbf{CO_2} +\ ^*\mathbf{CO} +\ ^*\mathbf{O} \rightarrow 4Li^+ + 4e^- + 2CO_2(g) +\ ^*\mathbf{CO} +\ ^*\mathbf{O} \tag{2h}$$

$$4Li^+ + 4e^- + 2CO_2(g) +\ ^*\mathbf{CO} +\ ^*\mathbf{O} \rightarrow 4Li^+ + 4e^- + 2CO_2(g) +\ ^*\mathbf{CO_2} \tag{2i}$$

$$4Li^+ + 4e^- + 2CO_2(g) +\ ^*\mathbf{CO_2} \rightarrow 4Li^+ + 4e^- + 3CO_2(g) \tag{2j}$$

As can be observed from Figure 5(c) and Table S3, the dissociation of Li_2CO_3 was uphill for both the RuNi/CSC and Ru/CSC-based catalysts, signifying a thermodynamically unfavorable process of charging. Due to this, there was an observable overpotential in the charging process.

Further, the subsequent dissociation of the $^*CO_3$ to $^*CO_2$ and $^*O$ were thermodynamically favorable for the RuNi/CSC catalyst compared to the Ru/CSC catalyst, indicating the enhanced catalytic activity with the incorporation of Ni in the Ru lattice structure. Further steps involving the conversion of amorphous carbon to CO_2 had similar energy requirements for both catalysts. However, the second controlling step for the charging reaction involving the decomposition of another molecule of Li_2CO_3 into Li^+ ions and CO_2 had significantly lower reaction energies for RuNi/CSC catalyst than Ru/CSC, thus enabling better reversibility of the catalyst on charging. The enhanced catalytic activity by forming the nanoalloy alloy to ensure the reversibility of the discharge products explains the experimental observations of excellent electrochemical performance by the RuNi/CSC-based Li-CO_{2Mars} battery.

Conclusions

To conclude, we synthesized a RuNi nanoalloy alloy catalyst on the candle soot-based carbon substrate and utilized it to operate Li-CO_{2Mars} batteries efficiently. The batteries delivered a high discharge capacity of 15207 $mAhg^{-1}$ at a high current density of 200 mAg^{-1} and a high coulombic efficiency of nearly 99.3%, indicating the synergistic catalytic ability and the electron conducting ability of the candle soot-based carbon. When operated at an ultrahigh current density of 500 mAg^{-1}, the battery could be cycled up to over 100 cycles for a limited capacity of 500 $mAhg^{-1}$, further confirming the catalytic enhancement on the performance of the Li-CO_{2Mars} battery. The physical characterization studies demonstrated almost complete reversibility of the discharge products, indicating the efficient catalytic activity and its subsequent impact on the performance of Li-CO_{2Mars} batteries. Further from the DFT studies, it was observed that the formation of $^*Li_2C_2O_4$ intermediate was the kinetic rate-limiting step and was the possible reason for improving the system's operability even at higher current densities. Further, the lower energy required by the RuNi/CSC catalyst for the decomposition of the discharge products helps in the excellent reversibility of the cathode surface. The facile and scalable synthesis method, excellent cycling performance, high discharge capacity, and low overpotential make it a prospective choice for developing a practicable Li-CO_{2Mars} battery for interplanetary rover missions to Mars along with mitigating climate change on Earth through CO_2 capture and reduction.

Experimental Section

Chemicals and reagents

Ruthenium chloride hydrate (Sigma Aldrich), Nickel (II) nitrate hexahydrate (98% - ThermoFischer Scientific), lithium foil (99% - Sigma Aldrich), lithium bis(trifluoromethane sulfonyl)imide (LiTFSI) (99.95% - Sigma Aldrich), dimethyl sulfoxide (DMSO) (99.8% - Sigma Aldrich), N-methyl-2-pyrrolidone (NMP) (99.5% - Sigma Aldrich), polyvinylidene fluoride (PVDF - Sigma Aldrich), Ethylene glycol (99% - s d fine-chem (SDFCL)) and absolute, anhydrous, HPLC, Ethyl alcohol (Ethanol) (PHARMCO-AAPER) were used as it is. Glass microfiber filters separator (Whatman, GF/D; Global Life Sciences Solutions), carbon paper (RSI, India), candles from a local market, and Martian CO_2 gas (95% CO_2, 2.6% N_2, 1.9% Ar, 0.16% O_2 and 0.06% CO by volume, AGEM India) were used for this work.

Synthesis of RuNi/CSC catalysts

The candle soot nanocarbon was collected from the tip of the flame of a burning candle, followed by heat treatment in an air atmosphere to 450°C for 2 h to remove the wax impurities and enhance the purity of the carbon as per our previous studies.[28,30] The heat-treated candle soot was homogeneously dispersed ultrasonically in the ethylene glycol solvent. The precursors $RuCl_3 \cdot 3H_2O$ and $Ni(NO_3)_2 \cdot 6H_2O$ were mixed, and the resulting solution was stirred overnight for uniform distribution of the precursors into the solution. The obtained solution was then subjected to a solvothermal process in a Teflon-lined autoclave at a temperature of 180°C

Batteries & Supercaps

Research Article
doi.org/10.1002/batt.202300328

**Chemistry
Europe**

European Chemical
Societies Publishing

for 10 h. The resulting black precipitate was then centrifuged and washed with absolute ethanol and distilled water to remove the unreacted reactants, followed by freeze drying to remove the residual solvents. The freeze-dried sample was then subjected to heat treatment in a tubular furnace at 350 °C for 2 h in an Argon atmosphere to obtain the bimetallic nanoalloy catalyst RuNi/CSC. The control sample of Ru/CSC was prepared through the same procedure without adding Ni precursor.

Materials characterization

The structure of the materials was characterized with XRD patterns by using a Rigaku bulk material and powder XRD with CuKα ($\lambda=$ 1.54056 Å) radiation and 2θ ranges of 10° to 90°. The morphology was analyzed by FESEM images using a focused ion beam FESEM (JEOL JIB-4700F) at the acceleration voltages of 15 kV. The HR-TEM images were carried on a field emission TEM (JEOL JEM-2100) and JEOL F 200 cold FEG-TEM at the acceleration voltage of 200 kV. The surface analysis was carried out by XPS on a Kratos Axis Supra (Shimadzu) X-ray photoelectron spectrometer using a monochromated Al anode of Kα: 1486.69 eV. The XPS data were deconvoluted using XPSPEAK software. The ICP-OES studies were conducted in a Prodigy XP High Dispersion ICP-OES (Teledyne Leeman Labs). The R.F. power was maintained at 1.1 kW, and the nebulizer pressure was maintained at 25 psi. The wavelengths for the elements were aligned with an exposure time of 30 seconds. The sample uptake rate was 1.5 mL min^{-1} with an uptake time of 20 seconds. Nanobase xperRAM equipped with a 532 nm laser was used to take the Raman spectra of the samples. The measurements were taken with an average of 5 scans and an acquisition time of 20 s. The Quantachrome Autosorb iQ instrument was used to measure the catalyst's BET surface area with the help of the N$_2$ adsorption-desorption isotherms. The process consists of a degassing time of 8 h at 150 °C. The pore size distributions were measured with the non-local DFT method in the same equipment.

Electrode preparation and cell assembly

The cathode was prepared by slurry coating method on the carbon paper with a diameter of 15 mm. Typically, the coating material (slurry) was prepared by mixing 90 wt% of catalyst and 10 wt% of polyvinylidene fluoride (PVDF) in N-methyl-2-pyrrolidone (NMP) solvent and were blended to form a uniform slurry. The slurry was hand painted on a 15 mm diameter circular disk shape carbon paper (carbon paper, thickness 0.4 mm, porosity 78%, density 0.44 g cm^{-3}) and dried in a vacuum oven at 80 °C overnight. The catalyst-loaded carbon paper was used as a working electrode, with an active material loading of 0.3–0.4 mg cm^{-2}.

A CR2032-type coin cell Li-CO$_{2Mars}$ battery was assembled with holes on the cathode side in a glove box filled with high-purity Argon. Li foil (15 mm in diameter) was used as an anode, and glass fiber (19 mm in diameter) was used as a separator with 1.0 M LiTFSI and 0.3 M LiNO$_3$ in DMSO solvent as an electrolyte. Later, the assembled coin cell was sealed in a homemade bottle arrangement and purged with Martian gas (95% CO$_2$, 2.6% N$_2$, 1.9% Ar, 0.16% O$_2$, and 0.06% CO). The battery performances were examined at various conditions by using the potentiostat (Biologic BCS-805). The discharge-charge capacity in this work was calculated based on the mass loading of the catalyst on the electrode. The electrochemical impedance spectroscopy (EIS) analyses were performed in the frequency range of 10 kHz to 100 mHz with the same potentiostat. The discharged and charged electrodes were washed with DMSO to remove any residual LiTFSI salt before post-characterization of XRD, XPS, Raman, and FESEM measurements.

First-principles calculations

The density functional theory calculations were carried out by the Vienna Ab Initio Simulation Package (VASP).[31–33] The ion-electron interactions were described by the projector-augmented plane wave (PAW) approach using the generalized gradient approximation (GGA). The exchange-correlation functionals by Perdew, Burke, and Enzerhof were used.[34] The self-consistent-field calculations were allowed until the energy difference between the two iterations converged to within 1×10^{-4} eV with atomic forces smaller than 0.02 eV/Å. The plane wave cutoff energy for the wave function was set to 400 eV. A vacuum layer of 12 Å was added along the z direction to avoid the interactions between the periodically repeating units. The Brillouin zone was sampled using gamma-centered 4×4×1 Monkhorst-Pack k-points grids for structure optimizations. The adsorption energies (E_{ads}) were obtained using the following equation:

$$E_{ads} = E_{total} - E_M - E_I \tag{3}$$

E_{ads} represents the substrate's adsorption energy in eV, E_{total} represents the structure's total energy in eV, E_M represents the structural energy of RuNi/CSC in eV, and E_I represents the energy of the intermediate formed in eV. The optimized structures were visualized using VESTA software.[35]

Supporting Information

Additional references cited within the Supporting Information (Ref. [36–43]).

Conflict of Interests

The authors declare no conflict of interest.

Data Availability Statement

The data that support the findings of this study are available from the corresponding author upon reasonable request.

[1] IEA(2021), *World Energy Outlook*, IEA, Paris, https://www.iea.org/reports/world-energy-outlook-2021, **2021**, 32–35.

[2] "Energy and the environment explained Outlook for future emissions," can be found under http://www.eia.gov/energyexplained/energy-and-the-environment/outlook-for-future-emissions.php, **2021**, 8–10.

[3] M. Naranjo, D. T. Brownlow, A. Garza, *Energy Procedia* **2011**, *4*, 2716–2723.

[4] D. Berstad, R. Anantharaman, P. Nekså, *Int. J. Refrig.* **2013**, *36*, 1403–1416.

[5] Z. Z. Kecheng Pan, Minghui Li, Weicheng Wang, Shuochao Xing, Yaying Dou, Shasha Gao, Zhang Zhang, *Green Energy & Environ.* **2023**, *8*.

[6] M. Li, K. Pan, W. Wang, S. Xing, Y. Dou, Z. Zhang, Z. Zhou, *Batteries & Supercaps* **2023**, *n/a*, e202300230.

[7] Z. Zhang, L. Zhao, Z. Xie, Z. Zhou, *Green Chem. Eng.* **2020**, *1*, 79–81.

[8] A. K. Chourasia, A. D. Pathak, C. Bongu, K. Manikandan, S. Praneeth, K. M. Naik, C. S. Sharma, *Small Methods* **2022**, *6*, 2200930.

[9] Z. Lian, Y. Pei, S. Ma, Y. Lu, Q. Liu, *ChemistrySelect* **2022**, *7*, e202104549.

[10] X. Wang, H. Liu, Q. Wang, J. Huo, W. Ge, X. Duan, S. Guo, *Appl. Surf. Sci.* **2021**, *540*, 148351.

[11] Y. Xu, H. Gong, L. Song, Y. Kong, C. Jiang, H. Xue, P. Li, X. Huang, J. He, T. Wang, *Mater. Today Energy* **2022**, *25*, 100967.

[12] B. Chen, D. Wang, J. Tan, Y. Liu, M. Jiao, B. Liu, N. Zhao, X. Zou, G. Zhou, H.-M. Cheng, *J. Am. Chem. Soc.* **2022**, *144*, 3106–3116.

[13] H. Wu, Z. Wang, X. Zeng, Z. Fei, Y. Gu, K. Ding, P. Dong, Y. Zhang, Q. Meng, *Ceram. Int.* **2023**, *49*, 4153–4159.

[14] Y. Kong, H. Gong, L. Song, C. Jiang, T. Wang, J. He, *Eur. J. Inorg. Chem.* **2021**, *2021*, 590–596.

[15] H. Xie, B. Zhang, C. Hu, N. Xiao, D. Liu, *Electrochim. Acta* **2022**, *417*, 140310.

[16] P.-F. Zhang, Y.-Q. Lu, Y.-J. Wu, Z.-W. Yin, J.-T. Li, Y. Zhou, Y.-H. Hong, Y.-Y. Li, L. Huang, S.-G. Sun, *Chem. Eng. J.* **2019**, *363*, 224–233.

[17] L. Song, C. Hu, Y. Xiao, J. He, Y. Lin, J. W. Connell, L. Dai, *Nano Energy* **2020**, *71*, 104595.

[18] L. Fan, H. Shen, D. Ji, Y. Xing, L. Tao, Q. Sun, S. Guo, *Adv. Mater.* **2022**, *34*, 2204134.

[19] K. D. Gilroy, A. Ruditskiy, H.-C. Peng, D. Qin, Y. Xia, *Chem. Rev.* **2016**, *116*, 10414–10472.

[20] Z. Zhang, X.-G. Wang, X. Zhang, Z. Xie, Y.-N. Chen, L. Ma, Z. Peng, Z. Zhou, *Adv. Sci.* **2018**, *5*, 1700567.

[21] Y. Wang, J. Zhou, C. Lin, B. Chen, Z. Guan, A. M. Ebrahim, G. Qian, C. Ye, L. Chen, Y. Ge, Q. Yun, X. Wang, X. Zhou, G. Wang, K. Li, P. Lu, Y. Ma, Y. Xiong, T. Wang, L. Zheng, S. Chu, Y. Chen, B. Wang, C.-S. Lee, Y. Liu, Q. Zhang, Z. Fan, *Adv. Funct. Mater.* **2022**, *n/a*, 2202737.

[22] F. Zhong, Q. Wang, C. Xu, Y. Yang, Y. Wang, Y. Zhang, D. Gao, J. Bi, G. Fan, *Appl. Surf. Sci.* **2018**, *455*, 326–332.

[23] Y. Hou, J. Wang, L. Liu, Y. Liu, S. Chou, D. Shi, H. Liu, Y. Wu, W. Zhang, J. Chen, *Adv. Funct. Mater.* **2017**, *27*, 1700564.

[24] Z. Zhang, C. Yang, S. Wu, A. Wang, L. Zhao, D. Zhai, B. Ren, K. Cao, Z. Zhou, *Adv. Energy Mater.* **2019**, *9*, 1802805.

[25] Y. Liu, S. Zhao, D. Wang, B. Chen, Z. Zhang, J. Sheng, X. Zhong, X. Zou, S. P. Jiang, G. Zhou, H.-M. Cheng, *ACS Nano* **2022**, *16*, 1523–1532.

[26] S. Thoka, C.-M. Tsai, Z. Tong, A. Jena, F.-M. Wang, C.-C. Hsu, H. Chang, S.-F. Hu, R.-S. Liu, *ACS Appl. Mater. Interfaces* **2021**, *13*, 480–490.

[27] B.-W. Zhang, Y. Jiao, D.-L. Chao, C. Ye, Y.-X. Wang, K. Davey, H.-K. Liu, S.-X. Dou, S.-Z. Qiao, *Adv. Funct. Mater.* **2019**, *29*, 1904206.

[28] A. K. Chourasia, A. Shavez, K. M. Naik, C. Bongu, C. S. Sharma, *ACS Appl. Energ. Mater.* **2023**, *6*, 378–386.

[29] J. Hu, C. Yang, K. Guo, *J. Mater. Chem. A* **2022**, *10*, 14028–14040.

[30] D. Potphode, C. S. Sharma, *J. Energy Storage* **2020**, *27*, 101114.

[31] G. Kresse, J. Furthmüller, *Phys. Rev. B* **1996**, *54*, 11169–11186.

[32] G. Kresse, J. Furthmüller, *Comput. Mater. Sci.* **1996**, *6*, 15–50.

[33] G. Kresse, J. Hafner, *Phys. Rev. B* **1993**, *47*, 558–561.

[34] J. P. Perdew, K. Burke, M. Ernzerhof, *Phys. Rev. Lett.* **1996**, *77*, 3865–3868.

[35] K. Momma, F. Izumi, *J. Appl. Crystallogr.* **2011**, *44*, 1272–1276.

[36] Y. Jin, F. Chen, J. Wang, *ACS Sustainable Chem. Eng.* **2020**, *8*, 2783–2792.

[37] K. V. Savunthari, C.-H. Chen, Y.-R. Chen, Z. Tong, K. Iputera, F.-M. Wang, C.-C. Hsu, D.-H. Wei, S.-F. Hu, R.-S. Liu, *ACS Appl. Mater. Interfaces* **2021**, *13*, 44266–44273.

[38] S.-L. Chou, S.-X. Dou, *Matter* **2020**, *2*, 1356–1358.

[39] Z. Zhang, W.-L. Bai, Z.-P. Cai, J.-H. Cheng, H.-Y. Kuang, B.-X. Dong, Y.-B. Wang, K.-X. Wang, J.-S. Chen, *Angew. Chem. Int. Ed.* **2021**, *60*, 16404–16408.

[40] Y. Qiao, J. Wu, J. Zhao, Q. Li, P. Zhang, C. Hao, X. Liu, S. Yang, Y. Liu, *Energy Storage Mater.* **2020**, *27*, 133–139.

[41] Q. Deng, Y. Yang, S. Qu, W. Wang, Y. Zhang, X. Ma, W. Yan, Y. Zhang, *Energy Storage Mater.* **2021**, *42*, 484–492.

[42] G. Yue, X. Luo, Z. Hu, W. Xu, J. Li, J. Liu, R. Cao, *Chem. Commun.* **2020**, *56*, 11693–11696.

[43] A. Bharti, G. Manna, P. Saha, G. Achutarao, A. J. Bhattacharyya, *J. Phys. Chem. Lett.* **2022**, *13*, 7380–7385.